Effects of vessel-pipe coupled dynamics on the discharged CO_2 behavior for CO_2 sequestration

Farid P. Bakti[*] and Moo-Hyun Kim

Department of Ocean Engineering, Texas A&M University, College Station, Texas, USA

Abstract. This study examines the behaviors and properties of discharged liquid CO_2 from a long elastic pipe moving with a vessel for the oceanic CO_2 sequestration by considering pipe dynamics and vessel motions. The coupled vessel-pipe dynamic analysis for a typical configuration is done in the frequency and time domain using the ORCAFLEX program. The system's characteristics, such as vessel RAOs and pipe-axial-velocity transfer function, are identified by applying a broadband white noise wave spectrum to the vessel-pipe dynamic system. The frequency shift of the vessel's RAO due to the encounter-frequency effect is also investigated through the system identification method. Additionally, the time histories of the tip-of-pipe velocities, along with the corresponding discharged droplet size and Weber numbers, are generated for two different sea states. The comparison between the stiff non-oscillating pipe with the flexible oscillating pipe shows the effect of the vessel and pipe dynamics to the discharged CO_2 droplet size and Weber number. The pipe's axial-mode resonance is the leading cause of the fluctuation of the discharged CO_2 properties. The significant variation of the discharged CO_2 properties observed in this study shows the importance of considering the vessel-pipe motions when designing oceanic CO_2 sequestration strategy, including suitable sequestration locations, discharge rate, towing speed, and sea states.

Keywords: CO_2 sequestration; fluid-structure interaction; system identification; vessel-pipe coupled dynamic analysis, pipe axial vibration, resonance, discharged fluid properties, operable sea state

1. Introduction

CO_2 storage or sequestration technology is a part of an integrated effort to reduce the harmful CO_2 emission released to the atmosphere from industrial-scale human activities. The captured CO_2 can conventionally be stored in the depleted oil & gas reservoir or can be used as EOR (enhanced oil recovery) catalyst in the oil & gas production. On the other hand, due to the abundance of storage capacity that the ocean offers, direct CO_2 injection into the deep portion of the ocean is also seriously considered as a potential solution in the last couple of decades (IPCC report, 2005).

One of the most common strategy that can be deduced from the oceanic CO_2 storage studies is the direct-controlled injection of CO_2 in the mid-depth, spreading the CO_2 over a large spatial domain. Consequently, the CO_2 becomes very diluted and turns into one with naturally occurring CO_2 circulation in the ocean-atmospheric system, thus reducing its harmful effects on its surrounding (IPCC report, 2005). The spreading method is done by towing a hanged discharge pipe

---

∗Corresponding author, Ph.D. Student, E-mail: faridputrabakti@gmail.com

from a ship, as shown in Fig.. The injection depth has to be sufficient so that the CO_2 can be entirely dispersed in the seawater before they can reach the surface. To achieve it, the discharge depth is typically 800 m below the surface and is a function of the system's mixing properties (Socolofsky *et al.* 2008). The mixing properties are indirectly affected by the dynamics of the ship-pipe system.

The significance of the fluid-structure interaction in the oceanic CO_2 injection can be recognized when considering that, on both dissolution and lake type injection, the discharge pipes are configured to be hanging 800 – 2500 m from the surface vessel. These configurations would mean that the vessel motions might cause a noticeable dynamic disturbance along the whole length of the pipe, especially at the tip of the pipe, where the discharge nozzle is typically located. This structural dynamic process can then affect the mixing parameters of CO_2 in the ocean, such as its thermodynamic properties, ambient turbulent kinetic energy, dissolution rate of the CO_2, and the droplet or bubble size of the discharged CO_2. Due to the complexity of the fluid-structure interaction throughout the CO_2 injection process, the direct relationship between the disturbance at the vessel and the change in CO_2's mixing parameters is considered to be the most practical design parameter.

Jeong *et al.* (2010) demonstrated a 3D numerical simulation of a dissolution type CO_2 injection method from a moving ship by considering hypothetical operational conditions. The injection was done from 30 moving ships or injection points, and the liquid CO_2 discharge depths were varied from 1500 to 2500 m below the surface. However, the study neglected the fluid-structure interaction that might affect the discharged fluid behavior. As shown by previous studies (e.g., Marshall *et al.* 1986; Pilch *et al.* 1987, Ozaki *et al.* 2001), the relative fluid velocity between the discharge nozzle and the ambient fluid can affect the discharged bubbles behaviors, which in turns, can change the dissolution rate and plume's influence area (Socolofsky *et al.* 2008).
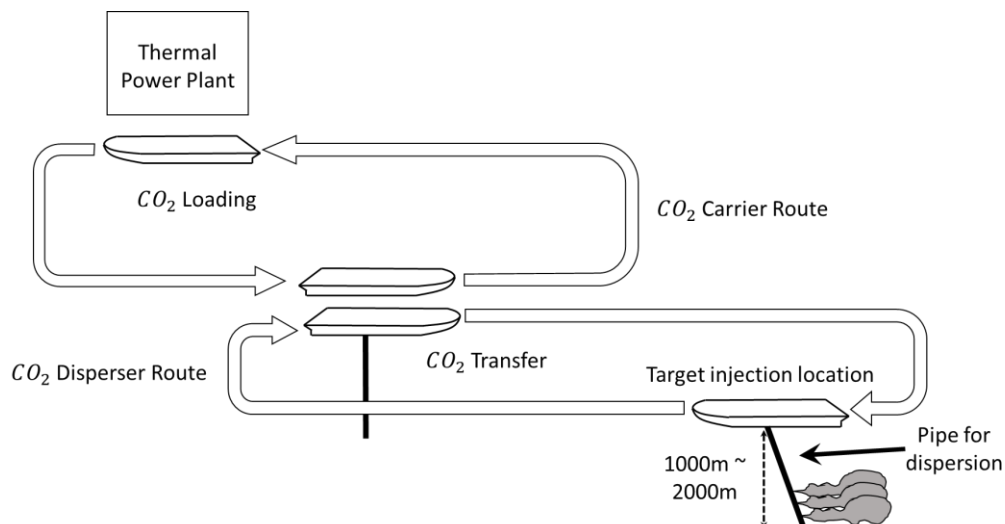
Fig. 1 Dissolution type injection method (Ozaki *et al.* 1997)
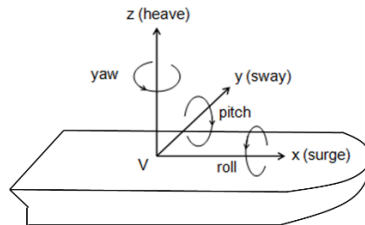
Fig. 2 Definition of the vessel's degrees of freedom
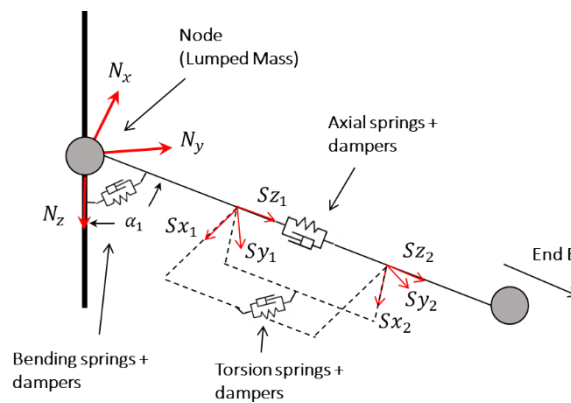
Fig. 3 Line-pipe model (Orcina 2012)

2. Methodology

2.1 Vessel – pipe coupled dynamics

The vessel that is used for the present CO_2 sequestration study is a repurposed tanker ship. The vessel's 6DOF (degrees of freedom) response amplitude operator (RAO) can be calculated using a boundary element program, such as WAMIT (Lee *et al.* 1991, Wamit inc.), where the vessel's geometry and mass matrix are used as the input. The program can also calculate the added mass, hydrostatic stiffness, and radiation damping. The vessel's degrees of freedom are shown in Fig. 2.

The vessel-pipe coupling dynamics are solved using the time-domain finite element simulation ORCAFLEX (Orcina 2012). It is necessary to do the coupled dynamics simulation in time-domain, to take into account the nonlinearity in the system. Furthermore, because the RAO of the vessel is given for zero forward speed, the time-domain simulation can approximate the system's RAO for non-zero forward speed.

The line is modeled as a lumped mass and spring-damper system for translational and rotational degrees of freedom (Fig. 3). The hydrodynamic force acting on the line is modeled using the Morison's equation. The corresponding mass-damping-stiffness-forcing matrices are then combined with the vessel's matrices, and they are solved simultaneously in the time domain. The governing equation of motion is given below (Ran and Kim 1997, Kim *et al.* 2005, Kim and Kim, 2015)

$$[M + M_a]\{\ddot{x}(t)\} + \int_{-\infty}^{t} ([C(t - \tau)]\{\dot{x}(t)\})d\tau + [K]\{x(t)\} = \{F(t)\} \tag{1}$$

where $\{\ddot{x}\}, \{\dot{x}\}, \{x\}$ are acceleration, velocity, and displacement vectors, respectively for each degree of freedom. $[M]$ is the inertia matrix, and $[M_a]$ is the added mass at the infinite frequency for vessel's degrees of freedom and added mass from Morrison's equation for the line's degrees of freedom. The second term corresponds to the convolution integral with the retardation function $C(\tau) = \frac{2}{\pi}\int_0^{\infty} C(\omega)\cos(\omega\tau)\, d\omega$ with C as frequency-dependent radiation damping. For the line's degrees of freedom, the damping comes from the Morison's quadratic drag force. The $[K]$ matrix is the stiffness matrix; where for the vessel's degrees of freedom, it is the hydrostatic stiffness, while for line's degrees of freedom, it is pipe's bending and axial stiffness.

The Morrison's force equation is only applied to slender members, which in this study are the pipe elements, and it is defined as below

$$F_{morrison} = \rho\forall a + \rho C_a \forall(a - \ddot{x}) + \frac{1}{2}\rho A C_d(v - \dot{x})|v - \dot{x}| \tag{2}$$

where $\forall$ is the displaced fluid's volume, ρ is the fluid's density, C_a is the added mass coefficient, a is the fluid's local acceleration, A is the projected area normal to the flow, C_d is the drag coefficient, v is the fluid's local velocity. Through numerical integration and derivatives, the structure's position, velocity, and acceleration are solved by solving the corresponding sets of linear equations. The vessel-pipe coupling effects are represented in the system's matrix as follows.
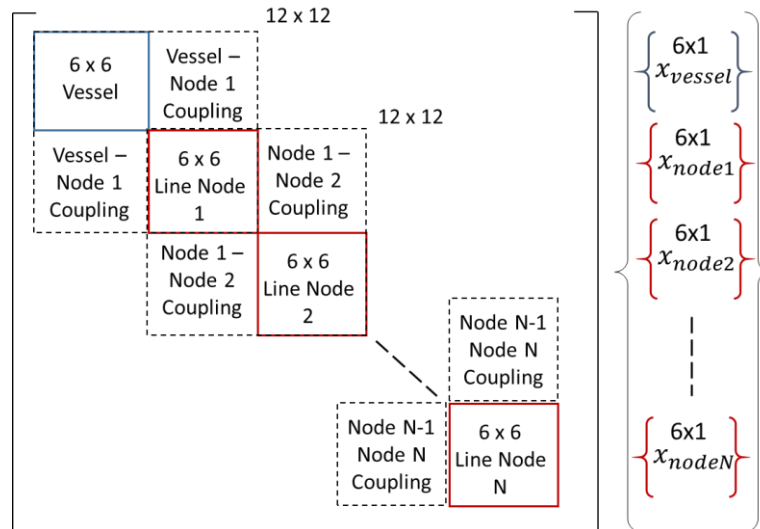
Fig. 4 Vessel-pipe coupling method as system matrices

2.2 System identification

The corresponding system identification is carried out by running the time-domain simulation of the vessel-pipe system with the input white-noise (uniform amplitude) wave spectrum. The analysis is done to reveal the intricate interaction among the input wave, the vessel's dynamics, and the pipe's dynamics. However, in this work, the final response result of the pipe/line velocity at the nozzle location is assumed to be linearly dependent with the inputted sea level elevation. This assumption makes it possible to find the frequency-dependent direct transfer function from the wave input to the velocity at the nozzle location. The transfer function can be obtained by dividing the output spectrum with the input spectrum. These process can be described by Fig. 5 below

The input is chosen to be broadband white noise spectrum so that the resulting response characteristics are clearly shown in the output spectrum. This approach is necessary since there is a possibility that important peak responses at higher or lower frequencies are not revealed in the case where there is no input energy at those frequencies.

Due to the presence of the forward speed and noises from the non-linear interaction inside the system, the output spectrum is expected to have a lot of high-frequency noise. Therefore, the Butterworth filtering technique was applied to the data to mitigate this noise.

2.3 Effect of the vessel-pipe motion to the fluid dynamics

Marshall *et al.* (1986) conducted an experiment on the turbulent crossflow liquid's effect on the dispersed air bubble injected from a small orifice under a particular pressure and temperature restriction. The sensitivity test of the orifice's dimension and the strength of the sweeping fluid's flow were also investigated to understand how the phenomena differ from the quiescent ambient fluid condition. The resulting equation that relates these parameters to the bubble size distribution is

$$D_{drp} = 1.72 - 0.682 \; |V_{cf}| + 0.556 \; ID_{nzl} + 0.00757 \; Q_i \tag{3}$$
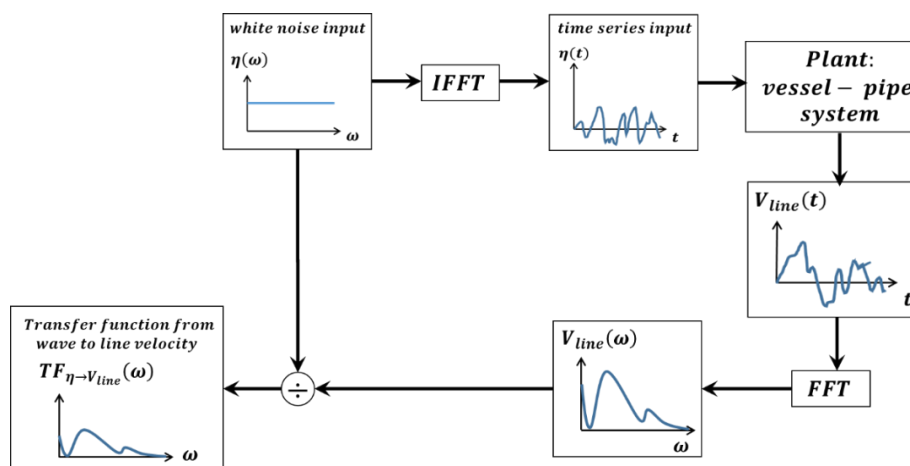
Fig. 5 System identification methodology
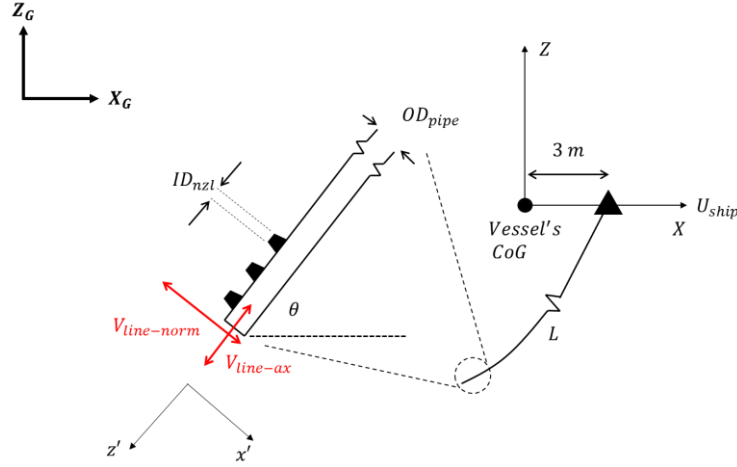
Fig. 6 Illustration of variables used in the present study

where D_{drp} is the mean bubble/droplet diameter in mm, V_{cf} is the crossflow velocity in m/sec, ID_{nzl} is the inner diameter of the output nozzle in mm, and Q_i is the volume flow rate of the discharged substance in ml/min. Small pored diffusers (0-5 mm diameters) were used to discharge the air bubbles. In the present study, the crossflow appears due to the relative velocity between the pipe's axial velocity ($V_{line-ax}$) and the ambient fluid, as illustrated as in Fig. 6.

Fig. 6 also shows the definitions of various variables used in the present study, where X_G is the earth fixed coordinate system, X is the ship fixed coordinate system, x' is the tip-of-pipe local coordinate system, L is the total pipe's length, OD_{pipe} is the outer diameter of the pipe, and θ is the final pipe angle after the target depth is reached. Both $V_{line-ax}$ and $V_{line-norm}$ are defined in the earth fixed coordinate system.

When compared to initial mean droplet size for stiff, non-oscillating discharge pipe, the ratio between the fluctuation in droplet size ΔD_{drp} can be formulated as follows:

$$D_{drp-stif} = 1.72 - 0.682 \; |U_{ship} \cos\theta| + 0.556 \; ID_{nzl} + 0.00757 \; Q_i \tag{4}$$

$$D_{drp-flex} = 1.72 - 0.682 \; |V_{line-ax}| + 0.556 \; ID_{nzl} + 0.00757 \; Q_i \tag{5}$$

$$\Delta D_{drp} = -0.682\{|V_{line-ax}| - |U_{ship} \cos\theta|\} = -0.682 \; \Delta|V_{cf}| \tag{6}$$

The above equation is obtained by considering that the only fluctuating variable in the system is the pipe's motion, while the others are constant. The time-domain simulation is conducted for the crossflow analysis since the absolute value of the crossflow terms in Eqs. (3)-(6) are non-linear. Also, we are interested in the statistical values, such as the mean and the maximum value, of the droplet size fluctuation. The mean value of the axial pipe fluctuation, in this case, coincides with $U_{ship} \cos\theta$ value.

Masahiko Ozaki *et al.* (2001) showed that the relative velocity between the discharge velocity and the towing velocity affected the type of droplets that were produced. The larger the relative velocity, the smaller the droplet size. Furthermore, Pilch *et al.* (1987) identified two important forces

governing the breakup of droplets, which are aerodynamic and surface tension forces. The ratio between these two forces are known as the Weber number

$$W_e = \frac{\rho_a V_a^2 D_{drp}}{\sigma} \tag{7}$$

where ρ_a is the ambient fluid's density, D_{drp} is the initial droplet diameter calculated using Eq. (3), σ is the surface tension, and V_a is the relative velocity between the droplets and the ambient fluid. Larger Weber number indicates the tendency for the droplet to break up into smaller sizes (Flock *et al.* 2012). For near field analysis, the V_a is approximately the same as the velocity magnitude of the discharged fluid, which can be formulated as follow

$$V_{a-flex} = \sqrt{\left(V_{line-norm} - \frac{Q_i}{A}\right)^2 + (V_{line-ax})^2} \tag{8}$$

$$V_{a-stif} = \sqrt{\left(U_{ship}\sin\theta - \frac{Q_i}{A}\right)^2 + \left(U_{ship}\cos\theta\right)^2} \tag{9}$$

where V_{a-flex} is the relative velocity for flexible oscillating pipe, V_{a-stif} is the relative velocity for stiff non-oscillating pipe, Q_i is the volume flow rate of the discharged CO_2 for each nozzle, A is the surface area of the nozzle opening, and $V_{line-norm}$ is the pipe's velocity in the normal direction (see Fig. 6). Pilch *et al.* (1987) categorized the breaking modes for Newtonian drops with Ohnesorge number less than 0.1 into five subcategories, which are,

3. System specification and configuration

Table 2 and Fig. 7 contain the vessel-related ORCAFLEX input data. From the RAO profile in Fig. 7, we can see that the surge and heave RAOs have the same local amplitude peaks at $=$ 0.15 Hz. The heave RAO has a second minor peak at $f = 0.2$ Hz. We can also see that both surge and heave RAOs converge to its maximum value of one as they approach $f = 0$ Hz. Meanwhile, the pitch RAO shows different behavior in that the maximum peak value occurred at $f = 0.1$ Hz and a second local peak at $f = 0.17$ Hz.

Table 1 Breaking modes for Newtonian drops

No breakup	$0 < W_e < {\sim}11$
Bag	${\sim}11 < W_e < {\sim}35$
Multimode	${\sim}35 < W_e < {\sim}80$
Sheet thinning	${\sim}80 < W_e < {\sim}350$
Catastrophic	$W_e > {\sim}350$

Table 2 Towing vessel properties

Variables	Definition	Values & Dimensions
L_p	Length between perpendicular	$103\ m$
B	Breadth	$15.95\ m$
D	Draught	$6.66\ m$
W_{ship}	Total weight	$8800\ te$
(I_{xx}, I_{yy}, I_{zz})	Moment of inertia	$(249, 5830, 5830)x10^3\ te/m^2$
(x_{cg}, y_{cg}, z_{cg})	Center of gravity	$(\ 2.53, 0, -1.97\ )\ m$
(K_{22}, K_{26}, K_{66})	Hydrostatic stiffness	$(14/m, 29/rad, 1000m/rad)10^3 kN$
U_{ship}	Towing velocity	$3\ m/sec$
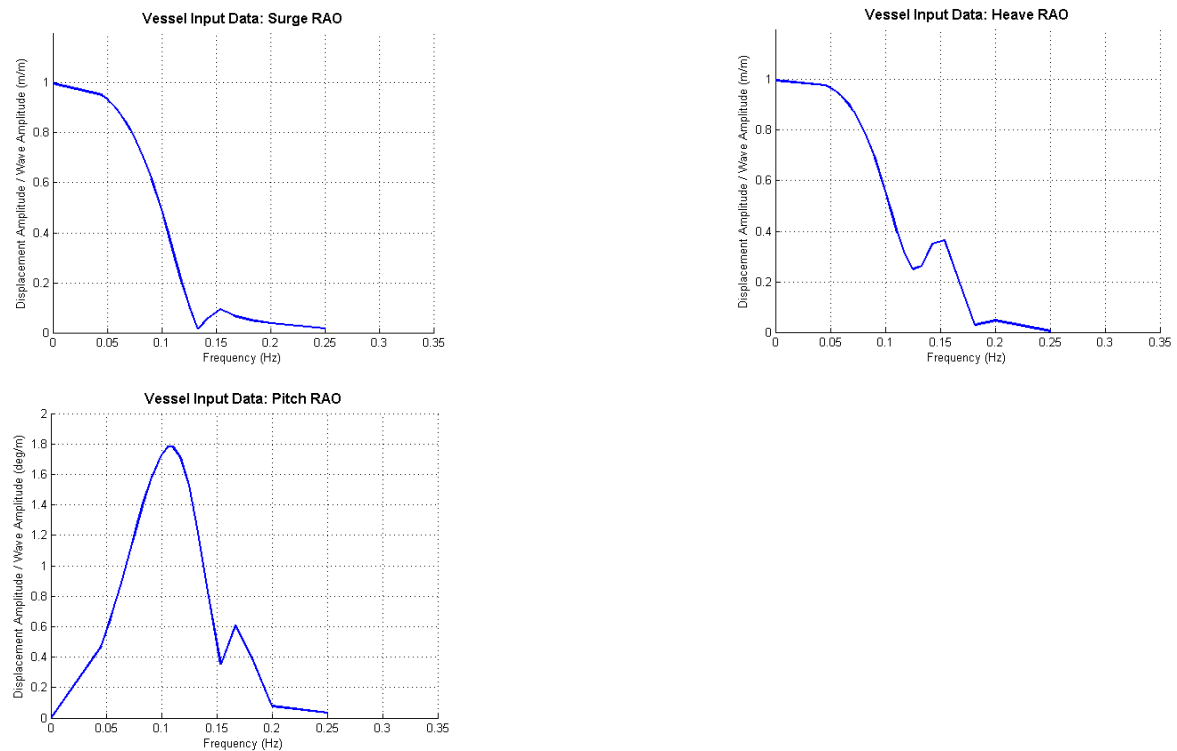
Fig. 7 Vessel's input surge, heave, pitch RAOs
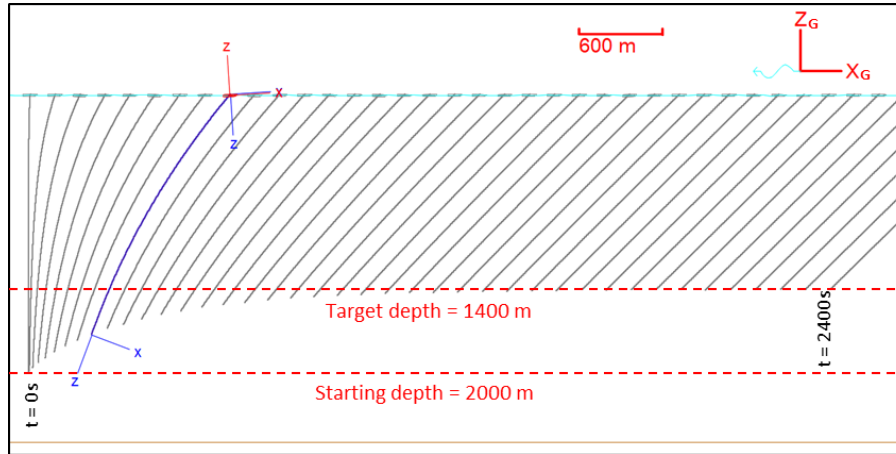
Fig. 8 Vessel – pipe configuration

Variables	Definition	Values & Dimensions
w_{pipe}	wetted weight of pipe / length	$0.15\ te/m$
L_{pipe}	The total length of the pipe	$2000\ m$
EA	Pipe's axial stiffness	$105x10^3\ kN$
EI	Pipe's bending stiffness	$94.3x10^3\ kN.m^2$
OD_{pipe}	Outer diameter of the pipe	$0.3\ m$
ID_{nzl}	Nozzle diameter	$5\ mm$
Q_i	The volume flow rate of the discharged CO₂	$500\ ml/min$
θ	Pipe's inclination angle at the target depth; $f(w_{pipe}, OD_{pipe}, U_{ship}.)$	44.43^0 or $0.78\ rad$
h_{target}	Target depth	$1400\ m$

The discharged pipe related data can be found in Table 3, while the evolutions of the vessel-pipe configuration without waves (no vessel and pipe oscillations) can be found in Fig. 8. All the frequency domain and statistical results are calculated after the tip-of pipe reached the target discharge depth of 1400 m, which is achieved after 2400sec.
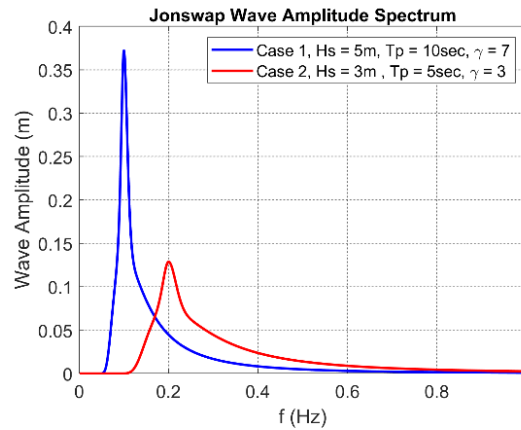
Fig. 9 Wave input JONSWAP spectrum

For the present mean bubble size study, two different JONSWAP random-wave spectra, as defined in Fig. 9, are simulated. Case 1 with $T_p = 10 \sec, Hs = 5\ m,$ and $\gamma = 7$ represents swell condition, while Case 2 $T_p = 5 \sec, Hs = 3m,$ and $\gamma = 3$ represents operational condition (Sea State 3). Both cases are for the head-sea condition. Notice that the peak frequency of Case 1 coincides with the peak frequency of the input pitch RAO.

4. Results and discussions

4.1 Structural dynamics' system identification

The vessel's RAOs with forward speed (Fig. 10) shows that the whole RAO is shifted to the right (higher frequency), and the peak amplitude is somewhat decreased. It is expected behavior due to the Doppler effect by the vessel's velocity, called encounter frequency in head waves. The surge local peak is shifted to $f = 0.2\ Hz$, the heave local peak is shifted to $f = 0.2\ Hz$ and $f = 0.28\ Hz$, and the pitch local peaks are shifted to $0.13\ Hz$ and $f = 0.23\ Hz$. Because of these shifts, the pitch peak frequency does not coincide with the input-spectral peak frequency of Case 1 anymore. However, the local peak frequencies of the surge and heave now coincide with the input spectral peak frequency of Case 2.

Fig. 11 shows the line's axial VTF obtained from system identification analysis. We can see that the VTF has three distinct local peaks located at f=0.1 Hz,0.2 Hz,0.3 Hz. The second peak at f=0.2 Hz coincides with the peaks of heave and surge RAOs, marking the coupling effect between the pipe and the ship. The influence of the vessel pitch motion is minimal since the injection pipe is connected to the longitudinal center of the ship. On the other hand, the first and last peak (around 0.1 Hz and 0.3Hz) of the pipe's axial velocity is not related to any local peaks of input wave or vessel-motion spectra.
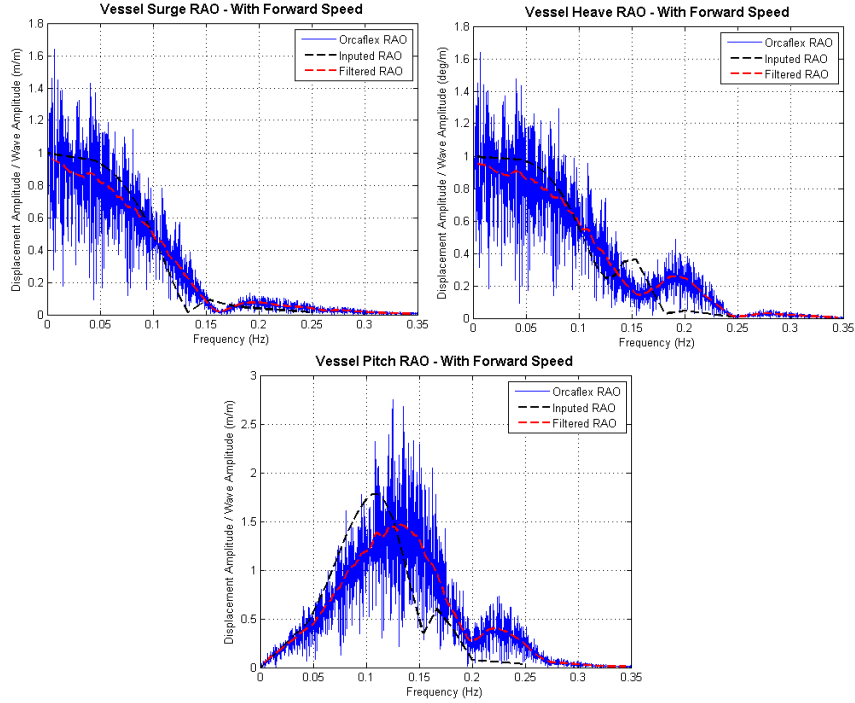
Fig. 10 System identification result of vessel's RAO with forward speed
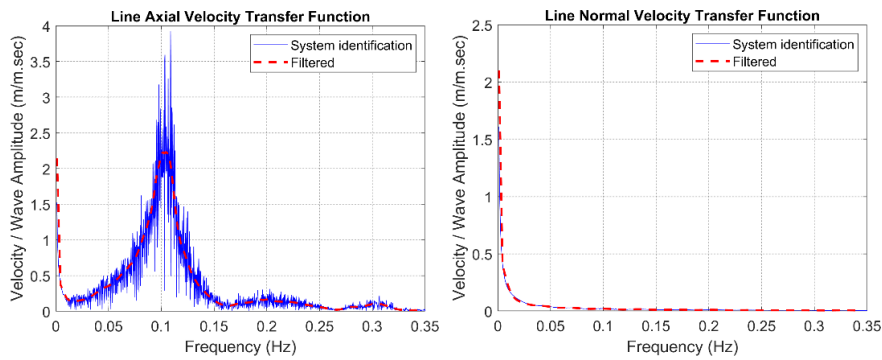
Fig. 11 Line's axial and normal Velocity Transfer Function (VTF) from system identification

The first and last local peaks in Fig. 11 can be explained if we account for the elastic modes of the pipe's dynamic. The axial mode's natural frequency of the pipe can be formulated as

$$f_{ax} = \frac{(2n-1)}{2\pi \ L} \sqrt{\frac{w_{pipe}}{EA}} = 0.1 \ Hz, 0.3 \ Hz, 0.5 \ Hz, ... \qquad n = 1, 2, 3, ... \qquad (10)$$

(a) CASE 1   (b) CASE 2
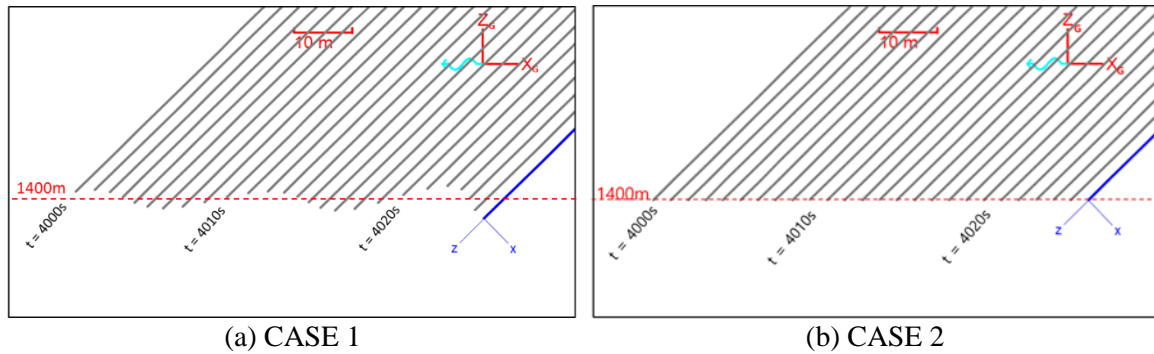
Fig. 12 Discharge pipe's position evolutions for two different sea states

The natural frequencies of the pipe's first and second axial modes are $f_{ax} = 0.1\ Hz$ & $0.3\ Hz$, which coincide with the first and third peaks of Fig. 11. With these results, it is clear that the velocity of the line is affected by the vessel's surge, heave, and pipe's axial elastic modes. As for Orcaflex results, it is also found that the bending modes of the pipe have little effect on the pipe's in-line velocity because they occur at much higher frequencies.

The random wave simulation results are shown in Figs. 11-13 while the statistical values of the line's velocity at the nozzle location are shown in Table 4. Both normal and axial pipe's velocity in the random wave simulations are consistent with the VTF characteristics in Fig. 10. Resonance with the pipe's first axial mode is clearly shown in the Case 1 results, causing a significant fluctuation in both tip-of-pipe position and velocity. On the other hand, Case 2 shows minor pipe's oscillations, even though its T_p coincides with the vessel's surge and heave local peaks. Therefore, it can be deduced that the elastic modes of the pipe are more dominant than the vessel's motion in determining the tip-of-pipe dynamics. The random wave simulation results also show that the pipe's oscillation in the normal direction is negligible for both cases. The time histories of the line's velocity can then be used to calculate the bubble/droplet related parameters in the following section.

Table 4 Statistical values of the line's velocity at the nozzle location

Velocity Component	Case Name	Maxima	Minima	Mean	Range	Standard Deviation σ
$V_{line-norm}$	Case 1	2.11	2.09	2.10	0.02	0.00
(m/sec)	Case 2	2.11	2.09	2.10	0.02	0.00
$V_{line-ax}$	Case 1	3.07	-7.24	-2.14	10.3	1.55
(m/sec)	Case 2	-1.87	-2.41	-2.14	-4.27	0.07
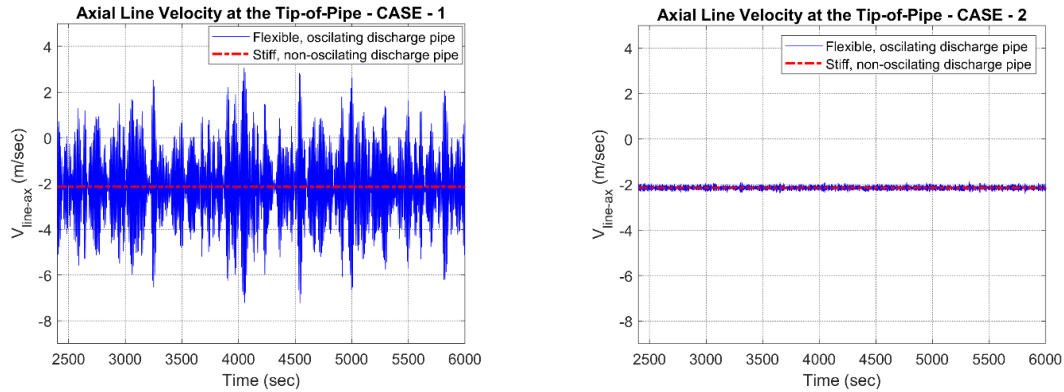
Fig. 13 Axial line velocity time history at the tip-of pipe for two different sea states
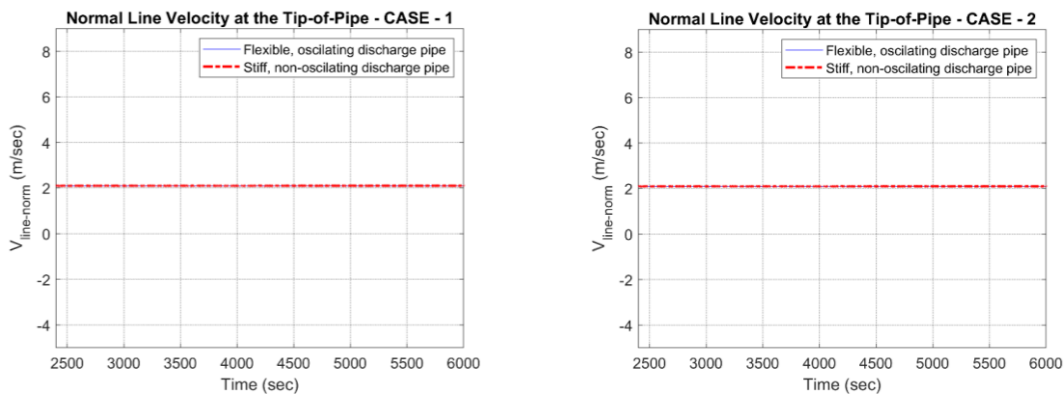
Fig. 14 Normal line velocity time history at the tip-of pipe for two different sea states

4.1 Effect of structural dynamics to the initial bubble size and Weber number

In Fig. 15, -100% is the minimum boundary in which the discharged bubble's diameter becomes zero (no discharged bubbles). Meanwhile, 0% $\Delta D_{drp}/D_{drp-stiff}$ means that there is no difference in the bubble sizes between the case where the motion of pipe-vessel is considered and the case in which the pipe is towed in a horizontal direction without waves. Any positive value means that the pipe-vessel motion due to wave excitation increases the initial droplet size.

From the same figure, we can also see that for the CASE-2, in which there is no pipe dynamics resonance, the vessel-pipe motions only cause a ±4% difference in the discharged bubble/droplet size. However, for some extreme cases such as CASE-1, the vessel-pipe motion can decrease the droplet size up to 70% in magnitude (see Table 5). This kind of significant fluctuation, therefore, cannot be neglected when calculating the initial droplet size. Since the majority of the fluctuation happens to decrease the discharged bubble/droplet size, the injected CO$_2$ would be dispersed quicker

than initially designed, and it will potentially change the resulting CO_2 concentration distribution profile. Eventually, this will affect the decision-making process when choosing suitable sequestration locations, including discharge rate, towing speed, and sea states.

Fig. 16 shows the Weber number of the flow very close to the nozzle where the ambient fluid velocity is approximated by Eqs. (8) and (9). For the less extreme case of CASE 2, the structural dynamics only cause a $\pm9\%$ change on the Weber number. However, In CASE 1, the Weber numbers are increased up to 114% of the original number when structural dynamics are not considered. Depending on the fluid's density and surface tension, the We fluctuation would mean that the breaking modes change from sheet thinning mode (We ~ 300) with no structural dynamics to catastrophic mode (We~540) with structural dynamics. However, this might not be meaningful if the Weber number is already extremely small or large in the first place.

From the bubble-size and the Weber number calculation, it is clear that Case 1 shows a much higher fluctuation than Case 2. This indicates that the incident-wave frequency plays a much more critical role than the wave amplitude, and that the pipe's axial mode has a larger effect in the process compared to the pipe-vessel coupled modes. The higher We and larger D_{drp} decrement than its increment indicates that the actual droplet size discharged from a moving ship is likely to be significantly smaller than the design droplet size without considering vessel-pipe dynamics.

Table 5 Statistical values of the discharged CO_2 initial droplet size and Weber number

Variables	Case Name	Maxima	Minima	Mean	Range	Standard Deviation σ
$\dfrac{\Delta D_{drp}}{D_{drp-stiff}}$	Case 1	29.6 %	-70.4 %	-1.6 %	100 %	19 %
	Case 2	3.8 %	-3.6 %	0.0 %	7.5 %	0.9 %
$\dfrac{\Delta W_e}{W_{e-stiff}}$	Case 1	114.1 %	-39.2 %	10.1 %	153.3 %	42.6 %
	Case 2	9.5%	-9.1 %	0.0 %	18.6 %	2.3 %
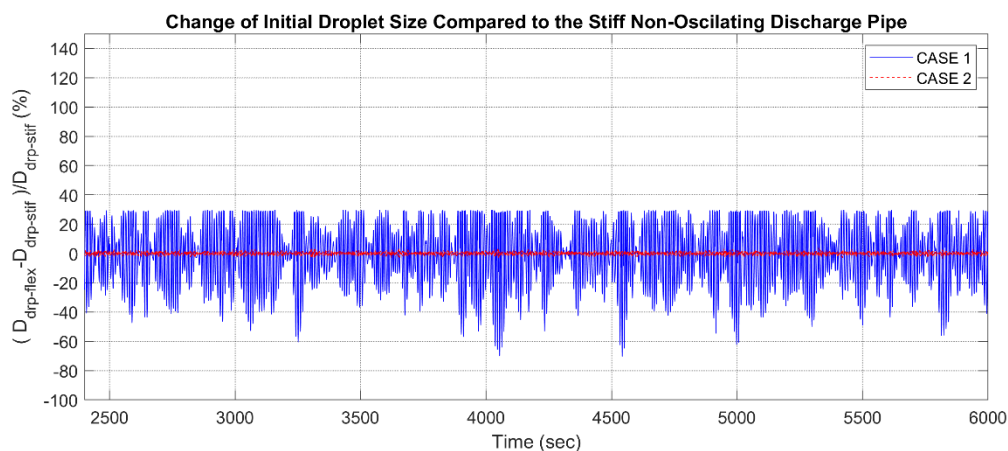
Fig. 15 Change of the discharged CO_2 droplet sizes for two different sea states
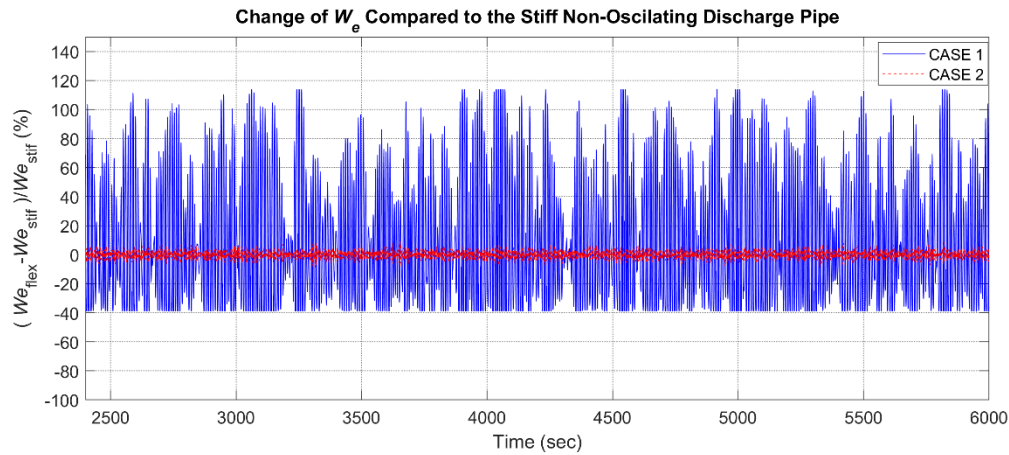
Fig. 16 Change of the discharged CO_2 Weber numbers for two different sea states

5. Conclsions

A system identification to examine the coupled vessel-pipe dynamics in the CO_2 sequestration application was conducted by utilizing both frequency-domain and time-domain analyses. The forward-moving vessel's RAO peaks are shifted to higher frequencies due to the encounter frequency effect. The line's axial velocity transfer function (VTF) showed distinct amplitude peaks at the resonance frequencies of pipe's axial modes, where the second peak (0.2Hz) coincided with the vessel's surge and heave local peaks. Since the VTF's first peak dominates all the other peaks, the pipe's axial oscillation is dominated by the corresponding pipe's elastic modes rather than by the vessel-pipe coupling.

From the random wave simulations, there exist significant differences in the line's axial velocity, bubble/droplet size fluctuation, and Weber number fluctuation, between the stiff and flexible pipes. The most significant difference was found in CASE-1, where the input wave's frequency coincided with the pipe's lowest natural frequency of axial vibration. On the other hand, the pipe's normal velocity at the tip-of-pipe location was little changed regardless of different wave conditions. In Case-1, the line's axial fluctuation can cause up to 70% decrease in the droplet size and up to 114% increase in the Weber number. These results indicate that the discharged droplet size is likely to be significantly smaller than the designed droplet size without considering vessel and pipe dynamics, therefore causing quicker CO_2 dispersion.

Therefore, the encounter frequency effect needs to be accounted for along with vessel and pipe dynamics when choosing the operational sea states. The discharged CO_2 velocities and properties can be quite different from the initial expectation without considering those effects. Eventually, both the encounter frequency effect and vessel-pipe dynamics need to be accounted for in the decision-making process when choosing suitable sequestration locations, discharge rate, towing speed, and sea states.

Acknowledgments

References

Flock, A.K., Guildenbecher, D.R., Chen, J., Sojka, P.E. and Bauer, H.J. (2012), "Experimental statistics of droplet trajectory and air flow during aerodynamic fragmentation of liquid drops", *Int. J. Multiphase Flow*, **47**, 37-49.

Intergovernmental Panel on Climate Change (2005), "Carbon dioxide capture and storage", *Cambridge University Press.*

Jeong, S., Sato, T., Chen, B. and Tabeta, S. (2010), "Numerical simulation on multi-scale diffusion of CO_2 injected in the deep ocean in a practical scenario", *Int. J. Greenhouse Gas Control*, **4**, 64-72.

Kim, M.H., Koo, B.J., Mercier, R.M. and Ward, E.G. (2005), "Vessel/mooring/riser coupled dynamic analysis of a turret-moored FPSO compared with OTRC experiment", *J. Ocean Eng.*, **32**, 1780-1802.

Lee, C.H., Newman, J.N., Kim, M.H., and Yue, D.K.P. (1991), "The computation of second-order wave loads", *Proceedings of the 10th International Conf.* OMAE Stavanger, Norway.

Marshall, S.H., Chudacek, M.W. and Bagster, D.F. (1986), "An initial study of air bubble formation from an orifice swept by transverse liquid flow", *Fluid Mech. Conf. Proc.*, **9**, 391-394.

Orcina (2012), Orcaflex user's manual – version 10.0.

Ozaki, M., Fujioka, Y., Takeuchi, K. and Sonoda, K. (1997), "Length of vertical pipes for deep-ocean sequestration of CO_2 in rough seas", *Energy*, **2**, 229-237.

Ozaki, M., Minamiura, J., Kitajima, Y., Mizokami, S., Takeuchi, K. and Hatakenaka, K. (2001), "CO_2 ocean sequestration by moving ships", *J. Mar. Sci. Technol.*, **6**, 51-58.

Pilch, M. and Erdman, C.A. (1987), "Use of breakup time data and velocity history data to predict the maximum size of stable fragments for acceleration-induced breakup of a liquid drop", *Int. J. Multiphase Flow*, **13**(6), 741-757

Ran, Z. and Kim, M.H. (1997), "Non-linear coupled responses of a tethered spar platform in waves", *J. Offshore Polar Eng.*, **7**(2), 111-118.

Socolofsky, S.A. and Bhaumik, T. (2008), "Dissolution of direct ocean carbon sequestration plumes using an integral model approach", *J. Hydraul. Eng.*, **134**(11), 1570-1578

Wamit Inc, "WAMIT 6.2 User Manual".

PS